Powder Technology 441 (2024) 119816

Contents lists available at ScienceDirect

Powder Technology

journal homepage: www.journals.elsevier.com/powder-technology

Milling amorphous FeSiB ribbons with vibratory ball and disc mills

Rosa María Aranda [a,*], Raquel Astacio [b], Petr Urban [b], Beatriz Aranda [a], Francisco G. Cuevas [a]

[a] Department of Chemical Engineering, Physical Chemistry and Materials Science, Escuela Técnica Superior de Ingeniería, Universidad de Huelva, Campus El Carmen, Avda. Tres de marzo s/n, 21071 Huelva, Spain
[b] Department of Materials and Transportation Engineering and Science, Escuela Técnica Superior de Ingeniería, Universidad de Sevilla, Camino de los Descubrimientos s/n, 41092 Seville, Spain

HIGHLIGHTS

- Production of amorphous powder by mechanical milling of ribbon.
- Use of vibratory disc and ball mill for $Fe_{78}Si_9B_{13}$ ribbon milling.
- Amorphous powder with a d (0.5) = 47 μm in 150 min with a vibratory disc mill.
- Amorphous powder with a d (0.5) = 48 μm in 90 min with a vibratory ball mill.

GRAPHICAL ABSTRACT

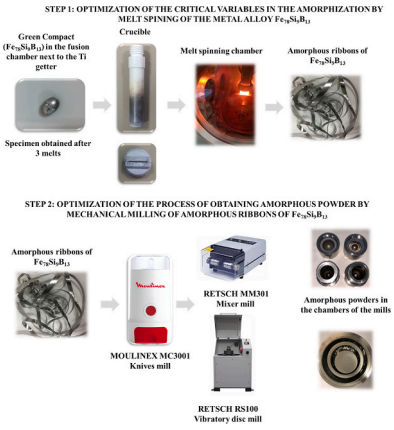

ARTICLE INFO

Keywords:
Melt spinning
Metglas alloy
Amorphization
Mechanical milling

ABSTRACT

Fe, Si and B powders, mixed with atomic composition $Fe_{78}Si_9B_{13}$, are subjected after arc melting to a melt spinning process, which is optimized to obtain the greatest amount of amorphous ribbon. The amorphous ribbons are milled to powder form in a vibratory ball mill and a vibratory disc mill, taking care of maintaining the amorphous character. Ribbons and powders have been characterized by X-ray diffraction (XRD), laser diffraction, SEM and TEM microscopy, and differential scanning calorimetry (DSC). The amorphous character and particle size of the powders are characterized as a function of the mill charge and the milling time. It is shown that the use of the ball mill is appropriate for obtaining small quantities of amorphous or nanocrystalline powder, while the disc mill can process larger quantities of powder in a shorter time. The particle sizes obtained for milling times between 10 and 150 min range between 26 and 412 μm, ready for use in powder metallurgy processes.

* Corresponding author.
E-mail address: rosamaria.aranda@dqcm.uhu.es (R.M. Aranda).

https://doi.org/10.1016/j.powtec.2024.119816
Received 19 February 2024; Received in revised form 11 April 2024; Accepted 28 April 2024
Available online 29 April 2024

Table 1
Review of milling of Fe-base amorphous ribbons. (BRR = Ball – Ribbons ratio; AM = Amorphous matrix; RT = Room temperature).

Alloy	Year	Mill	Vial / Balls	BRR	RPM	Atmosphere / T (°C)	Milling time	Powder size (μm)	Result – Time	Ref.
$Fe_{78}Si_9B_{13}$	1989	LS 10 K Glen Mills	–	–	–	–	–	250 μm	Fe_3B + α-Fe + AM –?	[39]
$Fe_{66}Co_{18}Si_1B_{15}$	1990	HEBM 8000 SPEX	Steel	–	–	– / RT	24 h	–	α-Fe(Co) + AM – 3 h α-Fe(Co) + $[Fe(Co)_2]B$ + AM – 12 h Crystalline – 24 h	[24]
$Fe_{78}Si_9B_{13}$	1990	HEBM 8000 SPEX	Steel	–	–	– / RT	24 h	–	α-Fe(Si) + AM – 3 h Nanocrystalline α-Fe(Si) – 24 h	[24]
$Fe_{72}Co_8Si_8B_{12}$	1992	HEBM 8000 SPEX	Steel	–	–	– / RT	24 h	–	α-Fe(Co) + $[Fe(Co)_2]B$ –? Crystalline – 24 h	[25]
$Fe_{65}Ni_{17}Si_7B_{11}$	1992	HEBM 8000 SPEX	Steel	–	–	– / RT	24 h	–	AM – 24 h	[25]
$Fe_{78}Si_9B_{13}$	1993	HEBM 8000 SPEX	Steel	4.5:1	–	Ar / RT Air / RT O_2 / RT	26 h	–	α-Fe(Si) + Fe_2B + AM – < 20 h Crystalline – 26 h α-Fe(Si) + Fe_2B + AM – < 4 h Crystalline – 5 h α-Fe(Si) + Fe_2B + AM – < 1.5 h Crystalline – 2 h	[26]
$Fe_{78}Si_9B_{13}$	1994	HEBM 8000 SPEX	Hardened Steel WC	5:1 20:1	–	Ar / RT	24 h	–	Traces of α-Fe(Si) + AM – 1.5 h α-Fe(Si) + Fe_2B + AM – 15 min	[35]
$Fe_{78}Si_9B_{13}$	1995	HEBM Attritor 01-I-ID Union Process 750	Stainless steel	100:1	–	N_2 / cryo.	100 h	–	Traces of α-Fe(Si) + Fe_2B + AM – 5 h Nanocrystalline α-Fe(Si) + Fe_2B – >100 h	[36]
$Fe_{77.2}Mo_{0.8}Si_9B_{13}$	1997	HEPBM WL-1	Stainless steel / Hardened steel	40:1	–	Ar / RT	307 h	–	AM – < 9 h Nanocrystalline α-Fe(Si) – 135 h	[40]
$Fe_{40}Ni_{40}P_{14}B_6$	1999	HEPBM	–	–	–	Ar / RT	90 h	–	AM – < 5 h Nanocrystalline γ-(Fe, Ni) + $(Fe, Ni)_3(P,B)$ – > 11 h	[41]
$Fe_{73.5}Cu_1Nb_3Si_{13.5}B_9$	2000	HEPBM WL-1	Stainless steel	25:1	240	N_2 / 4 °C	100 h	15 μm – 16 h 2–3 μm – 100 h	AM – < 16 h Nanocrystalline α-Fe(Si) – 100 h	[42]
$Fe_{77}Al_{2.14}Ga_{0.86}P_{8.4}C_5B_4Si_{2.6}$	2004	HEPBM PM4000 Retsch	Hardened steel	15:1	250, 200 and 150	Ar / RT	1 h	–	AM – 1 h	[43]
$Fe_{77}Al_{2.14}Ga_{0.86}P_{8.4}C_5B_4Si_{2.6}$	2004	HEPBM PM4000 Retsch	Agate	–	–	Ar / RT	10 h	300 μm	–	[44]
$Fe_{40}Ni_{40}P_xSi_{20-x}$ x = 10 or 14	2004	HEPBM P7 Frisch	–	50:1 30:1	350 (x = 10) 450 (x = 14)	Vacuum / RT	16 h (x = 10) 6 h (x = 14)	≥ 50 μm	Ni-rich silicides+ Fe-rich phosphides + Fe(Si) + Fe(Ni) + AM (x = 10) – 16 h AM (x = 14) – 6 h	[45]
$Fe_{78}Si_9B_{13}$	2005	HEBM 8000 SPEX	–	5:1	–	Ar / RT	–	50 μm 140 μm 350 μm	–	[46]
$Fe_{73.5}Cu_1Nb_3Si_{13.5}B_9$	2005	HEBM	Agate	10:1	–	Ar / RT	3.5 h	–	AM – < 2 h α-Fe + AM – > 2 h to <3.5 h	[47]
$Fe_{41}Ni_{20}Co_{20}Zr_7B_{12}$	2007	HEPBM P5 Frisch	Steel	–	250	Ar / RT	27 h	–	AM – < 27 h	[48]
$Fe_{73}Si_{16}B_7Nb_3Cu_1$	2007	Ball mill	Stainless steel	–	167	- / RT	36 h	60% wt < 45 μm	–	[49]
$Fe_{83}Zr_6B_{10}Cu_1$	2007	HEPBM P4 Frisch	Hardened steel	12:1	300	Ar / RT	24 h	250 μm – 2 h 50 μm – 6 h	α-Fe + AM – 2 h	[50]

(*continued on next page*)

Table 1 (*continued*)

Alloy	Year	Mill	Vial / Balls	BRR	RPM	Atmosphere / T (°C)	Milling time	Powder size (μm)	Result – Time	Ref.
$Fe_{73.5}Si_{16.5}B_6Nb_3Cu_1$	2007	HEPBM PM4000 Retsch	Hardened steel	7:1	200	Ar / RT	200 h	100–150 μm – 8 h –	α-Fe (Si) + AM – < 30 h (AM >90 wt% – 12 h) (AM >70 wt% – 30 h) Nanocrystalline α-Fe(Si) – 140 h	[51]
$Fe_{90}Zr_{10}$	2007	HEPBM AGO–2	Stainless steel	40:1	300, 400 600, 1000	Ar / RT	120 min		Nanocrystalline + residual AM – 30 min Crystalline – 30 min	[52]
$Fe_{78}Si_9B_{13}$	2008	HEPBM P6 Frisch	Stainless steel / Hardened steel	20:1	400	Ar / RT Air / RT	60 h	–	AM – < 8 h α-Fe(Si) + AM – > 8 h Nanocrystalline α-Fe(Si) – 24 h Nanocrystalline α-Fe(Si) + Fe_2B – > 24 h AM – < 3 h α- Fe(Si) + AM – > 8 h Nanocrystalline α-Fe(Si) – 30 h	[53]
$Fe_{77}Nb_7B_{15}Cu_1$	2009	HEPBM PM4000 Retsch	Hardened steel	15:1	200	– / RT	5 h	> 45 μm	α- Fe(Si) + AM – 5 h	[31]
$Fe_{81}Cu_2Nb_3Si_{14}$	2012	HEPBM QM – 3SP2	–	20:1	200	Ar / RT	2 h	150 μm	AM – 2 h	[54]
$Fe_{32}Ni_{52}Zr_3B_{13}$	2014	HEBM 8000 SPEX	Hardened steel	4:1	–	N_2 / RT	16 h	–	Fe(Ni) + AM – 30 min Fe(Ni) + $Zr_3Ni_{20}B_6$+ AM – 4 h Crystalline – 8 h	[55]
$Fe_{79.7\text{-}x}Nb_{0.3}Cr_xB_{20}$ (x = 11.5–13% at)	2014	HEPBM PM200 Retsch	Hardened steel	50:1	550	– / RT	90 h	1–3 μm – 10 h	α-Fe + AM – 6 h	[56]
$Fe_{80}Si_7B_{13}$	2014	HEBM Shaker-type milling	Stainless steel	4:1	–	Ar / RT	70 h	1 μm – 70 h	α-Fe + AM – 70 h	[57]
$Fe_{73.5}Si_{13.5}B_9Nb_3Cu_1$	2015	HEBM	Stainless steel	24:1	750	Ar / RT	65 min	–	α-Fe(Si) + AM – 24 min α-Fe(Si) + Fe_3B + Fe_2B + AM – 36 min	[33]
$[(Fe_{0.5}Co_{0.5})_{0.75}B_{0.2}Si_{0.05}]_{96}Nb_4$	2015	HEPBM P5 Frisch	WC	10:1	200	Ar/ RT	–	< 300 μm	–	[58]
$Fe_{73.5}Si_{13.5}B_9Nb_3Cu_1$	2015	HEBM	Stainless steel	24:1	750	Ar / RT	45 min	–	α-Fe(Si) + Fe_3B + Fe_2B + $Fe_{23}B_6$ + AM – 45 min	[59]
$Fe_{73.5}Si_{13.5}B_9Nb_3Cu_1$	2016	HEBM	Stainless steel	24:1	750	Ar / RT	45 min	7 μm – 45 min	α-Fe(Si) + Fe_3B + Fe_2B + $Fe_{23}B_6$ + AM – 45 min	[20]
$Fe_{80}Nb_{10}B_{10}$	2017	HEPBM PM400 Retsch	Hardened steel	10:1	200	Ar / RT	60 h	–	α-Fe(Si) + AM – 60 h	[60]
$FeCoNiSi_{0.4}Al_{0.4}$	2020	HEPBM QM – QX4		30:1	300	Ar / RT	60 h	–	–	[61]
$Sm_{10.5}Fe_{89.5}$	2020	HEBM 8000 SPEX	–	20:1	1725	Ar / RT	10 h	–	Sm_2Fe_9 + α-Fe + AM – 0.5 h Sm_2Fe_{17} + Sm_2Fe_9 + α-Fe + AM – 1 h α-Fe + AM – 2 to 5 h α-Fe – 5 h $SmFe_9$ + α-Fe + AM – ≥ 7 h	[62]
$Fe_{80}Si_1P_{10}C_9$	2022	HEBM 8000D SPEX	Hardened steel	1725	25:1	N_2 / - 90 °C - 50 °C	4 h	< 60 μm	AM – 4 h	[63]

1. Introduction

Amorphous metals are very attractive materials with outstanding properties. Mechanical [1], magnetic [2] or corrosion [3] behaviour, among others, can improve with the microstructural disorder of these materials.

Several methods can be considered to reach the intrinsically instable amorphous structure in metallic materials. These techniques are based on the extremely rapid cooling of a liquid to impinge ordering [4,5], atoms in vapour state deposited individually on a cold substrate [6], the disorder caused by ion irradiation [7], solid state reaction [8], or solid-state mechanical processes in which the internal structure of the materials is highly disordered [9].

Despite the final goal of any of these techniques is to obtain an amorphous structure, some other objectives should also be considered for specific uses. For instance, a high productivity, or obtaining a final

(a) (b)

Fig. 1. Image and detail of the vessels of (a) the vibratory ball mill, VBM and (b) the vibratory disc mill, VDM.

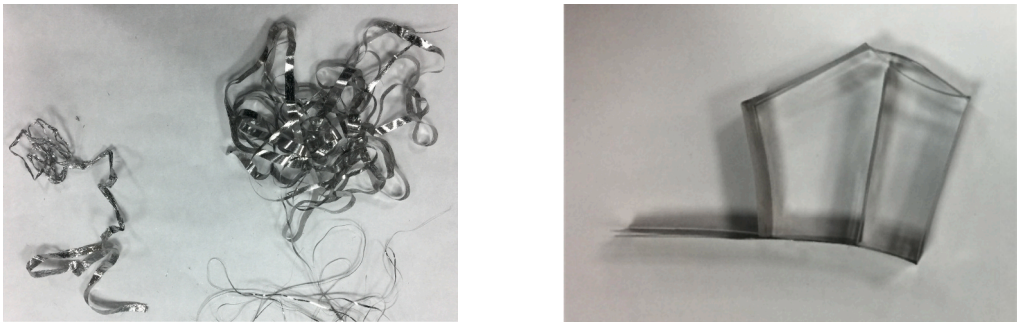

(a) (b)

Fig. 2. Image of **(a)** the melt spun $Fe_{78}Si_9B_{13}$ ribbon showing an initial inhomogeneous and a final well-formed zone, and (b) folded final part of the ribbon.

alloy without contamination, is always desirable. Thus, vapour deposition or ion irradiation are not much productive; mechanical alloying usually requires a process control agent to balance the welding and fracturing processes of the powder particles, remaining as impurity in the final composition of the powder; and the cooling rate of atomisation does not always get completely amorphous powders. The melt spinning process is therefore the most extended technique to produce amorphous materials, in form of ribbons, showing a high productivity and compositional control.

On the other hand, the amorphization process should on times finish in producing a bulk metallic glass (BMG) with the desired composition and geometry. However, obtaining BMGs is not always possible, being limited by the cooling rate that can be allowed for a particular composition at the time that the amorphous structure is maintained. For instance, soft magnetic materials with outstanding properties, obtained in amorphous state from Fe-Si-B-Nb-Cu alloys, can be obtained in bulk form with approximately a maximum diameter of 22 mm, but thicker sections irremediably produce crystalline structures [10,11]. In the search for Fe-based glasses with bigger dimensions, studies are being conducted using 3D printing technology such as the direct metal laser sintering process, with Fe-Cr-Mo-C-B alloys reaching a critical size of 45 mm [12]. Studying the glass forming ability and stability of new developed compositions is a tedious work, although artificial intelligence is now being used to make predictions [13].

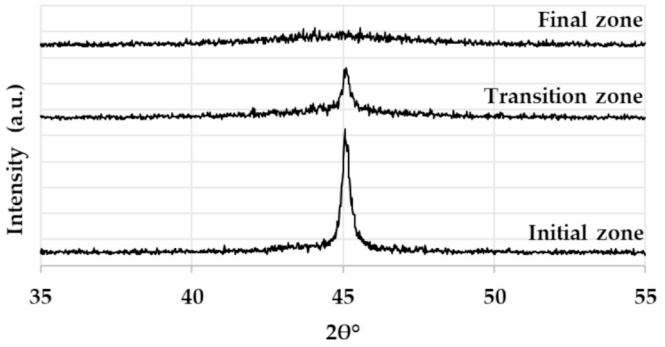

Fig. 3. XRD patterns of the initial, transition, and final zones of the melt spun $Fe_{78}Si_9B_{13}$ ribbons.

There are however other options to obtain BMGs, for instance, melt spun ribbons can be stacked to form the final shape, although this shape is generally as simple as a toroid. To form more complex shapes, it is possible to work with amorphous powders that must be mixed with an agglomerant [14]. If the presence of the agglomerant wants to be avoided, powders must be processed through powder metallurgy (PM) techniques. Unfortunately, the use of high or relatively high temperatures in traditional PM compromise the stability of the amorphous microstructure. Recently, field assisted sintering techniques (FAST), with the common characteristic of being very fast as compared to diffusive processes [15], have been considered. These techniques are based on the Joule heat generated by the passage of an electric current through the powder mass. Spark plasma sintering is the most extended technique, and it has been recently applied to consolidate amorphous Al-base [16–18] or Fe-base [19,20] powders. Nevertheless, much quicker techniques, with dwelling times in the order of seconds instead of minutes, as electrical resistance sintering [21] or capacitor electrical discharge [22], are also being considered.

For any of these FAST techniques to be applied, the appropriate powder particles in amorphous state and with the adequate granulometry is needed. Probably, the most extended way to obtain such impurity-free powders is by milling melt spun ribbons.

The study of the mechanical milling process of amorphous ribbons has been very intense in recent decades. The objective is not only to obtain amorphous powders, but also to understand the mechanical crystallization process produced by room temperature deformation [23], which leads to materials with specific microstructures. In general, crystallization achieved by heat treatments or mechanically initially results in a microstructure composed of nanocrystals embedded in an amorphous matrix, but there could be differences in the crystalline phases formed (which may or may not be beneficial for specific applications). Another difference is the difficulty to control the amount and size of the nanocrystals produced mechanically.

In 1989, Pak and Chu published the first study on the milling of Fe-base amorphous ribbons, but it was not until 1990 that Trudeau et al. carried out a systematic study on the crystallization of ribbons by milling [24]. $Fe_{66}Co_{18}Si_1B_{15}$ and $Fe_{78}Si_9B_{13}$ ribbons were milled in a high energy ball mill. The $Fe_{66}Co_{18}Si_1B_{15}$ ribbons required 24 h to reach the full crystallization (after the appearance of α-Fe(Co) at 3 h, and $Fe(Co)_2B$ after 12 h). In contrast, in the $Fe_{78}Si_9B_{13}$ alloy, after 24 h of milling, only the α-Fe(Si) phase was observed. Two years later, the same researchers studied the effect of the addition of Ni and Co, concluding that the addition of Co accelerated the crystallization process, and the presence of Ni slowed it down [25]. In addition, they studied the influence of the atmosphere used during the milling process, being the O_2 the one that quicker produced a mechanical crystallization, while the use of protective atmospheres, such as Ar, slowed down the crystallization process. In contrast, the presence of O_2 could inhibit the crystallization of some phases [26].

Since then, many researchers have followed this route to obtain amorphous as well as nanocrystalline or crystalline powders. A review of the research carried out in the last decades on mechanical milling of Fe-base amorphous ribbons is shown in Table 1. According to the literature, the process is mostly carried out in high energy mills with hardened steel or tungsten carbide vessels, under protective atmosphere (Ar or N_2), and with stop times to avoid high temperature during milling. On times cryogenic temperatures are used to help preserving the amorphous state [18,27]. Two types of high energy mills are the mostly used [28–30], ball mills (HEBM) and planetary ball mills (HEPBM). The average size of the powder particles obtained from these mills is in the range of 7–300 μm, most of them below 100 μm.

The use of HEPBM requires low ball-to-ribbon load ratios and low rotation speeds if the amorphous microstructure must be preserved. For instance, ratios between 15:1 and 5:1 and speeds between 150 and 200 rpm allow prolonging the milling of $Fe_{77}Nb_7B_{15}Cu_1$ ribbons up to 40 h while maintaining the initial microstructure [31,32]. Likewise, other compositions as $Ni_{59}Zr_{20}Ti_{16}Si_5$ retain the initial state after 9 h at a speed of 250 rpm and charge ratios of 10:1 and 5:1 [33]. With $Fe_{78}Si_9B_{13}$ ribbons, a charge ratio of 20:1 and rotational speed of 400 rpm allowed

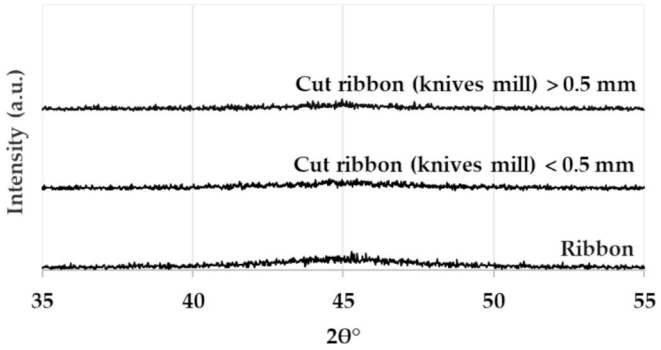

Fig. 5. XRD of the initial ribbon, and after cutting it in a knives mill for 3 min and sieved at sizes smaller and bigger than 0.5 mm.

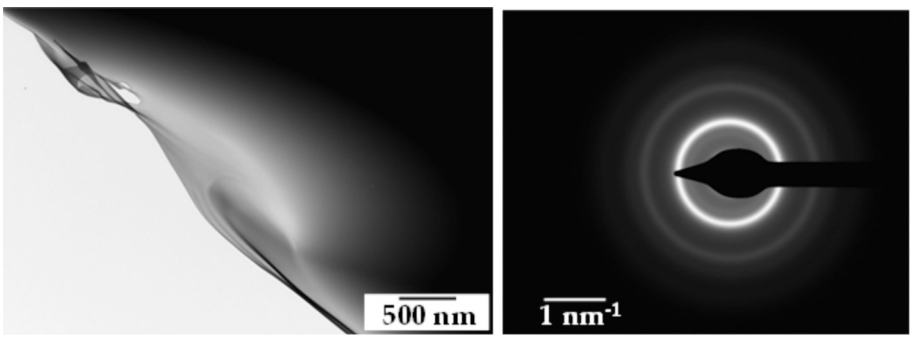

Fig. 4. TEM image and diffraction pattern of the melt spun $Fe_{78}Si_9B_{13}$ showing the amorphous structure of the final zone of the ribbon.

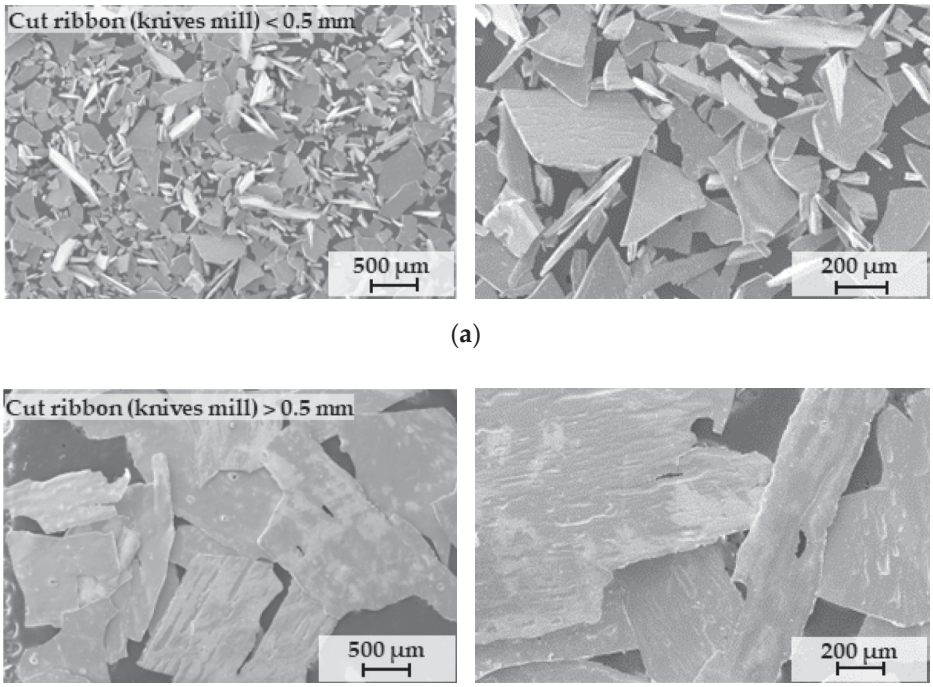

Fig. 6. SEM micrographs of the ribbons cut for 3 min in a knives mill: fraction with (**a**) particle size <0.5 mm; and (**b**) particle size >0.5 mm.

to obtain amorphous powders with milling times of up to 8 h in protective atmosphere, and <3 h in air. However, the higher energy achieved with a 24:1 ratio and 750 rpm can only be applied to Finemet ($Fe_{73,5}Si_{13,5}B_9Nb_3Cu_1$) ribbons for up to 24–36 min if the amorphous state must be preserved [20,34]. On the other hand, when using HEBM with amorphous $Fe_{78}Si_9B_{13}$ ribbons, with ratios of 20:1 and protective atmosphere, the milling time should be <1.5 h to preserve the initial microstructure [35], and with ratios of 100:1 and cryogenic temperatures the material is still amorphous after 5 h of milling [36].

Regarding the effect of milling on Fe-base alloys for magnetic applications, the presence of nanocrystals improves the thermal stability and enhances soft magnetic properties over its amorphous counterpart. In addition, a decrease in the size of the nanocrystals leads to a reduction in the coercivity of the material [37]. This behaviour was first observed for the partially nanocrystalline Finemet alloys, and later for the Nanoperm and Hitperm alloys. For instance, the Finemet alloy is obtained by annealing the amorphous alloy at a temperature between 480 and 550 °C for 1 h, resulting in the presence of α-Fe(Si) and a small amount of Fe_3Si crystals with sizes smaller than 10 nm in a weakly ferromagnetic Fe-Nb-B amorphous matrix. The material turns out to have excellent soft magnetic properties, largely dependent on the average size of the nanocrystals, and thus on the synthesis and annealing parameters [38].

However, other types of HEBM, as well as lower energy mills are also available, although are almost unexplored for these purposes. In this work, melt spun amorphous ribbons of Fe-Si-B were prepared and transformed to powder form by using two types of vibratory mills. The first one is a two-vessels ball mixer mill (vibratory ball mill, VBM) with a low ball-to-ribbon ratio (used range 2:1–1:1). On the other hand, a vibratory disc mill (VDM), whose operating principle can be likened in terms of energy to that of high-energy mills, has also been tested. The influence of the processing parameters on the powders obtained and their microstructure is analysed in this study, considering that maintaining the amorphous microstructure can result advantageous, because the nanocrystallisation process on times required to improve magnetic properties is better carried out, in general, by heat treating the amorphous powders.

2. Materials and methods

Elemental iron (ATOMET 1001HP, purity >99.4%, Rio Tinto, Montreal, Canada), silicon (Amperit 170, purity >99.6%, Flame Spray Technologies, Duiven, The Netherlands) and boron (Boron crystalline, purity >98%, Alfa Aesar, Schwerte, Germany) powders were mixed to give the desired composition of $Fe_{78}Si_9B_{13}$ (a simple composition of amorphous alloys known as Metglass [64]). The mix of 7 g of powder was pressed at 450 MPa to obtain a green compact 8 mm in diameter, valid to be arc melted. The arc melting process (Edmund Bühler MAM-1, Bodelshausen, Germany) was carried out in Ar atmosphere after Ti-gettering, and repeated for 3 times to obtain a homogeneous alloy. Ribbons were obtained by melt spinning (Edmund Bühler SC, Bodelshausen, Germany) using a rectangular nozzle of 0.4 × 10 mm^2 under different conditions: 1050–1250 °C with a wheel surface speed of 21–35 m/s, a nozzle-wheel distance of 0.3–0.7 mm and an ejection overpressure of 100–400 mbar in a chamber at 800 mbar.

The microstructure of melt-spun ribbons was examined with X-rays diffraction (XRD, Bruker D8 Advance, Allentown, United States) with Cu-Kα radiation and 2θ from 20 to 80° (only the range 35–55° is shown for more detail), and transmission electron microscopy (TEM, Philips CM200 at 200 KV, Amsterdam, The Netherlands). For TEM studies, specimens were prepared by precision ion polishing system (PIPS, Gatan 691, Pleasanton, CA, United States).

The thermal stability study of the ribbons was carried out in a differential scanning calorimeter (DSC, TA Instruments 2010, New Castle, DE, United States) with a heating rate of 20 °C/min under Ar atmosphere.

Selected zones of the ribbons, identified as amorphous, were then initially crushed in a knives mill (Moulinex MC3001, Lyon, France) for 3 min, and sieved fractions lower and higher than 5 mm were finally milled under different conditions: 3–6 g loads processed in a two-vessels VBM (Retsch MM301, Haan, Germany) with tungsten carbide ball (ball diameter 10 mm and ball weight 6 g, ball to powder ratio in the range

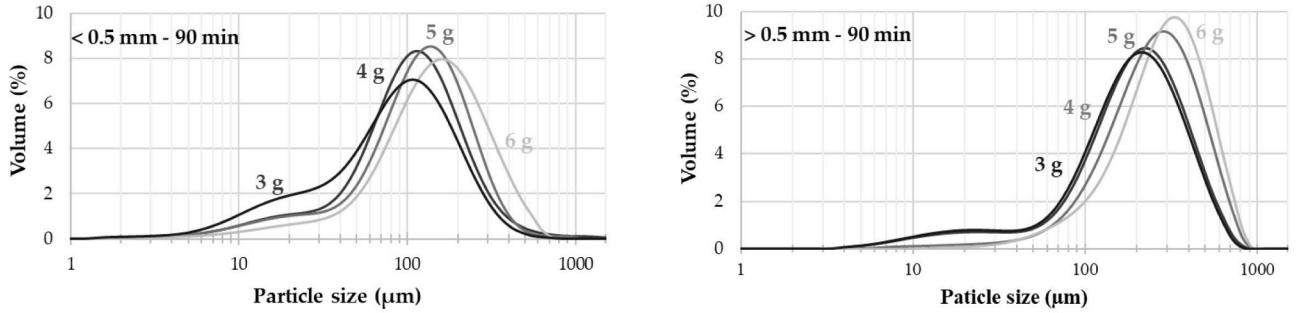

(a)

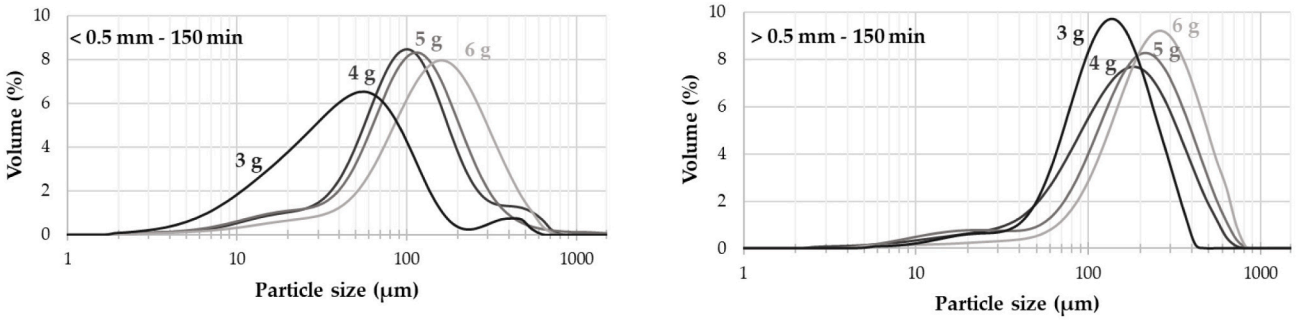

(b)

	d (0.5) (μm)							
d_i (mm)	< 0.5				> 0.5			
Load (g)	3	4	5	6	3	4	5	6
90 min	92 ± 5	113 ± 8	132 ± 7	157 ± 12	201 ± 15	212 ± 14	272 ± 15	311 ± 16
120 min	88 ± 3	102 ± 5	100 ± 3	139 ± 9	165 ± 12	172 ± 13	254 ± 14	273 ± 11
150 min	47 ±4	100 ± 4	113 ± 5	140 ± 6	112 ± 10	170 ± 9	201 ± 8	256 ± 10

(c)

Fig. 7. Granulometry of the powders obtained after milling in a mixer mill at 30 Hz for different loads and starting particles sizes, with milling times of: (**a**) 90 min; and (**b**) 150 min. (c) Detailed results for milling times of 90, 120 and 150.

2:1–1:1) and vial, for 30–150 min and vibrating frequency of 10 to 30 Hz; and 10–30 g loads processed in a VDM (Retsch RS100, Haan, Germany) with hardened steel disc and vial, for 10–150 min and vibrating frequency of 50 and 60 Hz (this makes the disc inside the milling reaching 700 and 1400 rpm respectively). Each milling time was studied independently, without extracting material of the mill at intermediate times. Fig. 1 shows the two types of mills used in this work.

Obtained powders were microstructurally and thermally characterized by XRD, scanning electron microscopy (SEM, Thermo Fisher Scientific FEI Teneo, Waltham, MA, United States), TEM, and DSC, and the granulometry by SEM and laser diffraction (Malvern Panalytical Mastersizer 2000, Malvern, UK). (The mean size values obtained from laser diffraction should be considered with care because of the flake shape of the powders and the measurement mechanism of this process).

The measurement of the absolute density of the powders is performed with a pycnometer (Accupyc II 1340, Micromeritics, USA). The tap density of the powders is determined according to the procedure followed in the ISO 3953:2011 standard [65]. The fluidity of the powders is determined from the Hall fluidimeter, following the procedure described in the ISO 4490:2011 standard [66]. The procedure followed to determine the compressibility of powders is that set out in the ISO 3927:2017 standard [67].

3. Results

3.1. Melt spinning process

Ribbons obtained in the melt spinner show two different zones for the studied composition (Fig. 2). The firstly formed part is inhomogeneous and brittle, with a typical thickness higher than 40 μm, whereas the final part is well-shaped and ductile, being possible to bend it up to 180° without breaking. The typical thickness of this zone varies between 17 and 35 μm depending on the processing conditions, always with a width of about 10 mm.

XRD shows that the initial zone of the ribbon is not amorphous, whereas the end is an amorphous material (Fig. 3). The transition zone between them shows an intermediate result in XRD.

Results obtained with XRD have been confirmed by TEM (Fig. 4). The amorphous microstructure is confirmed for the final zone of the ribbon.

Nevertheless, despite the aforementioned is the general behaviour for the melt spinning process, the processing parameter affect the results regarding the amorphous character, and the length of the final zone of the ribbon. Thus, high ejection pressures increase the flow on the wheel surface, resulting in thicker and more homogeneous ribbons, but thicker ribbons may result in nanocristalización of the material or complete loss of the amorphous character. Similarly, low wheel speeds result in better finished ribbons, although the amorphous character of the ribbon can be

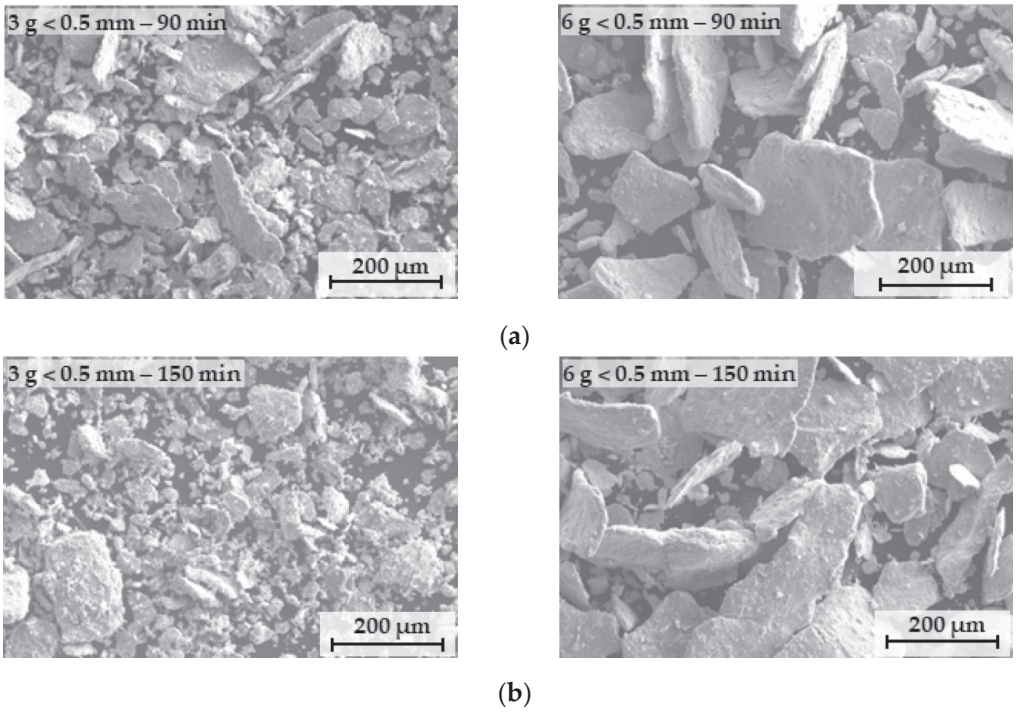

Fig. 8. SEM micrographs of cut ribbons smaller than 0.5 mm milled for (a) 90 min with a load in each vessel of 3 and 6 g and (b) 150 min with a load in each vessel of 3 and 6 g.

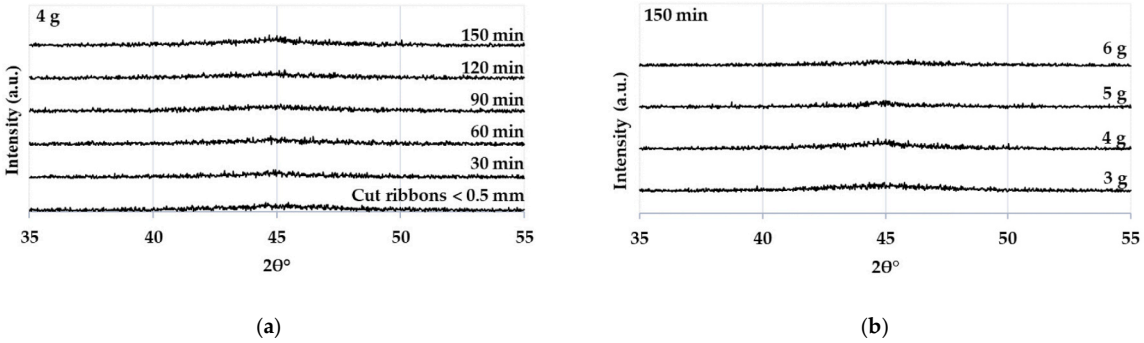

Fig. 9. XRD of milled ribbons <0.5 mm with: (**a**) a load of 4 g and milling times of 0 to 150 min; and (**b**) milling time of 150 min and loads of 3 to 6 g.

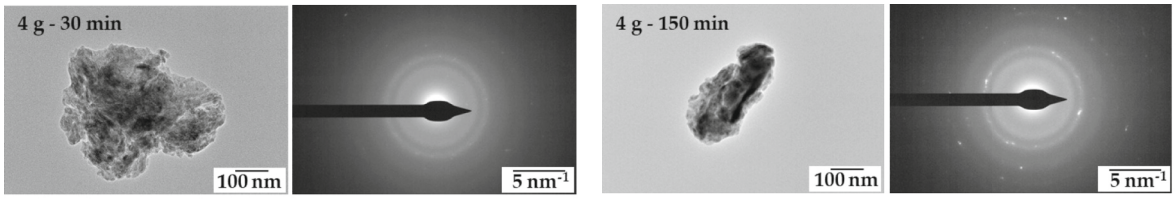

Fig. 10. TEM image and diffraction pattern of milled powders processed with a load of 4 g and a milling time of (**a**) 30 min and (**b**) 150 min (diffraction spots correspond to α-Fe).

compromised. For the maximum speed of 35 m/s the ribbons contain many voids and start to break up into narrower ribbons. Furthermore, high crucible-wheel distances and low ejection temperatures affect negatively to the quality of the ribbons.

From the above evidences, it is revealed that the optimum melt spinning conditions for the $Fe_{78}Si_9B_{13}$ alloy, with good amorphization according to XRD and TEM, is produced with a tank overpressure of 200 mbar, ejection temperature of 1250 °C, crucible - wheel distance of 0.4 mm and wheel speed of 28 m/s. With these conditions, used in the rest of this study, the process efficiency, measured as the amorphous fraction of the ribbon, reaches the 90%.

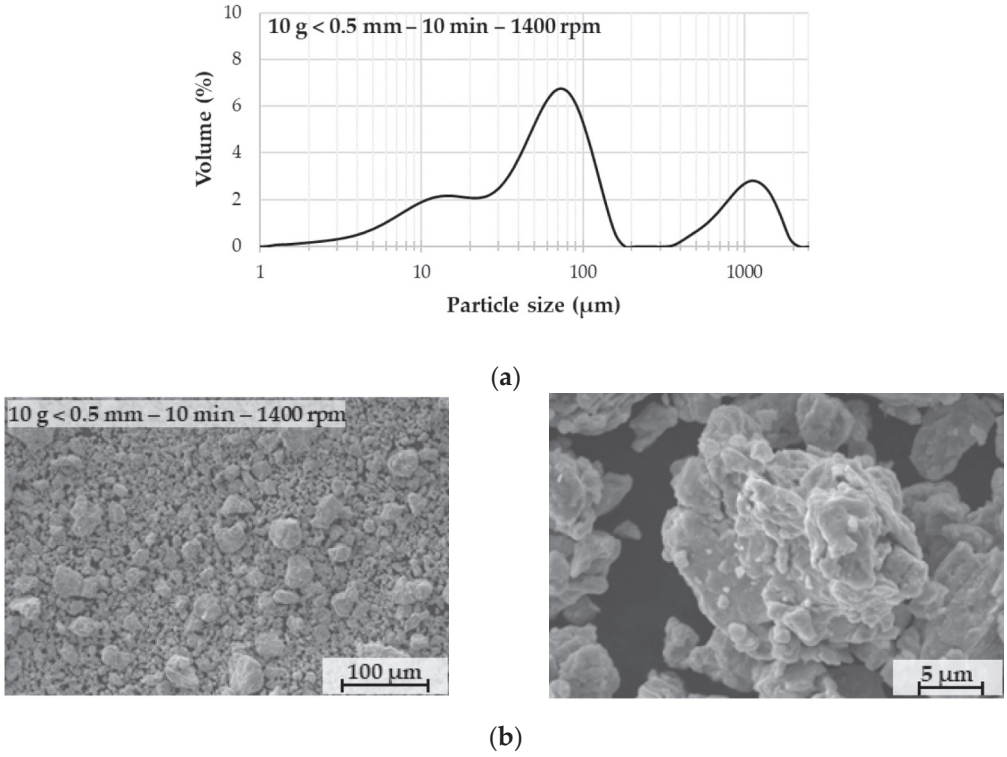

Fig. 11. (a) Granulometry and (b) SEM micrographs of a 10 g sample of cut ribbons <0.5 mm milled at 1400 rpm for 10 min.

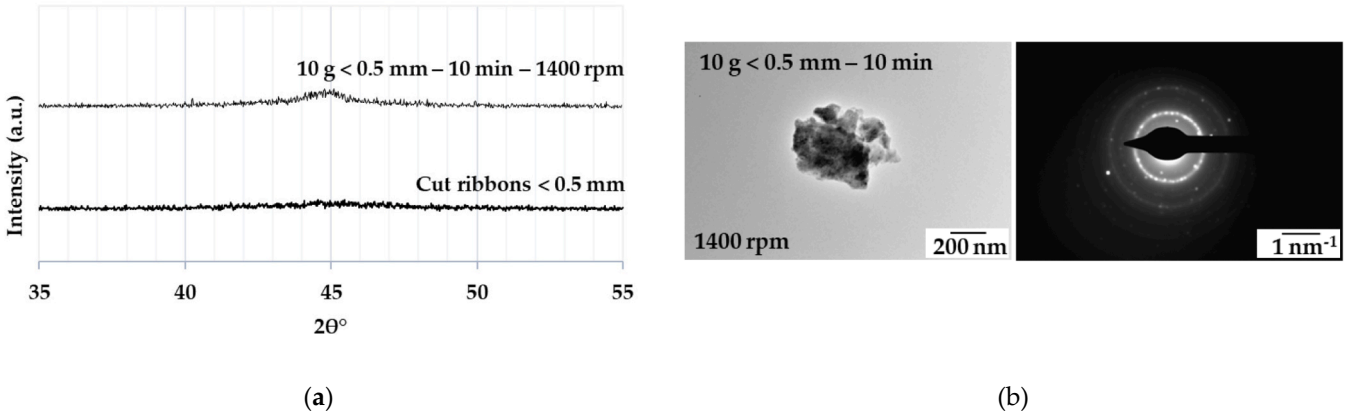

Fig. 12. (a) XRD of knives cut ribbons sieved at sizes lower than 0.5 mm and powders obtained after milling in a vibratory disc mill with 10 g load, milling time 10 min and 1400 rpm; (b) TEM image and diffraction pattern of the powder milled for 10 min, with a load of 10 g and a rotation speed of 1400 rpm.

3.2. Amorphous ribbon milling processes

3.2.1. Manual fragmentation and cutting in a knives mill

The ribbons are manually fractured to pieces of about 10 mm and processed in a knives mill for 3 min. The cut ribbons are then sieved to separate the fractions smaller and bigger than 0.5 mm. This is carried out to ensure a greater homogeneity in the granulometry of the powders to be finally obtained. XRD results verify that, due to the low energy of the process, there are no significant microstructural changes with respect to the original ribbons, and the cut ribbons remain completely amorphous in both cases (Fig. 5).

The morphological study by SEM (Fig. 6) shows that the cut ribbons adopt a flakes-shaped morphology, with mean sizes according to laser diffraction of 387 and 625 μm respectively, and the actual sizes that can be seen in Fig. 6.

3.2.2. Vibratory ball mill, VBM

It was first checked that frequencies of 10 and 20 Hz were insufficient to significantly reduce the particle size even for very long milling periods (tested times of up to 90 min), so, all experiences were carried out with a frequency of 30 Hz. The ball-to-ribbon load ratios were: for 3 g 2:1, for 4 g 3:2, for 5 g 6:5 and for 6 g 1:1. It was also found that, at this frequency, it was necessary to stop for 10 min every 30 min of milling, to avoid an excessive increase of the temperature in the vessels that could alter the amorphous microstructure of the starting material.

Fig. 7 shows the particle size obtained for some milling times as a function of the vessel load and the starting cut ribbons size (results for other milling times follow the same trend). As expected, higher milling times and lower loads in the vessels, make the particle size to decrease. The size distribution has a similar shape for the different experiences, but for low loads and starting particle size of <5 mm, a wider size

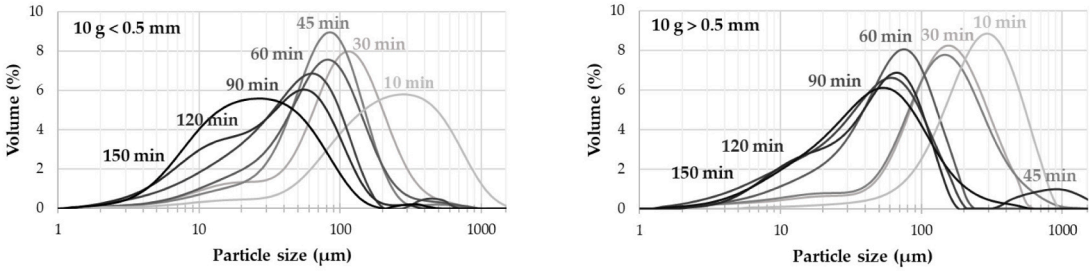

(a)

	d (0.5) μm		
d_i (mm)	**< 0.5 mm**		**> 0.5 mm**
Load (g)	**10**	**30**	**10**
10 min	241 ± 5	412 ± 16	278 ± 14
30 min	108 ±12	262 ± 9	158 ± 15
45 min	81 ± 11	123 ± 7	146 ± 12
60 min	74 ± 12	94 ± 13	135 ± 12
90 min	48 ± 9	92 ± 16	114 ± 16
120 min	35 ± 9	65 ± 8	56 ± 10
150 min	26 ± 3	51 ± 6	47 ± 4

(b)

Fig. 13. (a) Granulometry of the powders milled at 700 rpm for different milling times and starting sizes, with loads of 10 g. (b) Detailed results for milling times between 10 and 150 min.

distribution is observed, shifted towards smaller sizes, due to the greater effectiveness of the process. In addition, a second peak is observed for loads of 3 and 4 g, milling time of 150 min and initial particles size smaller than 0.5 mm, due to the agglomeration of the smaller particles.

The minimum mean particle size obtained is d(0.5) = 47 μm, and the maximum is d(0.5) = 400 μm, with an efficiency of the milling process (in terms of recovered material) of around 99% in all the cases.

The morphological study by SEM (Fig. 8) shows that the milled powder maintains, in general, the form of flakes, and only with long milling times and low load, the particles lose their initial morphology and become rounded.

The morphology, density, fluidity, and compressibility are important parameters to consider in PM processes. At this respect, the amorphous powders obtained are in the form of flakes obtained by the fracture of the original ribbons, although particles tending to become rounded are also observed when prolonging the milling. The absolute density ranges from 6.99 g/cm^3 (bigger powders, with mean size of 311 μm) to 6.81 g/cm^3 (mean size of 47 μm) and the tap density from 2.53 g/cm^3 (mean size of 311 μm) to 2.59 g/cm^3 (mean size of 47 μm). It is worth noting the difference between the absolute density measurements. The difference could be due to factors such as the formation of surface oxides by prolonging the milling time, or, more likely, to defects introduced in the amorphous structure itself, or simply to variations associated with the size of the powders. In any case, the values fall within the expected range, since a crystalline solid solution should have a density around 7.35 g/cm^3, and by a law of mixtures of the three components the value should be 7.36 g/cm^3. Being an amorphous structure, a lower value in the order of 5% is expected [68]. On the other hand, the literature reports values such as 7.1 g/cm^3 for amorphous ribbons in the $Fe_{80}Si_9B_{11}$ alloy [69]. The powders obtained do not flow and show compressibility curves typical of hard materials. At 1300 MPa the relative density varies between an 83% (mean size of 311 μm) and a 74% (size of 47 μm). Densification is higher with powders of larger mean size, which may be due to the better accommodation of the flake-shaped powder particles and their higher ductility.

These results, despite could be better in aspects as the fluidity, should be considered adequate for PM processing, as reported by other researchers [20,31,34,46,70]. For instance, Torrens-Serra et al. manufactured soft magnetic parts by hot pressing $Fe_{77}Nb_7B_{15}Cu_1$ amorphous milled ribbons, reaching relative densities of up to 94%, resulting in coercivities in the order of 40 A/m [31], or Gheiratmand et al. [20] fabricated Finemet bulk parts from amorphous milled ribbons by using SPS, reaching a relative density of 97% and coercivities in the order of 120 A/m.

The powders microstructure has been analysed by XRD as a function of the load and milling time (Fig. 9). The amorphous character is almost completely preserved even with prolonged milling times. For the case of milling the cut ribbons <0.5 mm for 150 min, and low vessel loads, it is observed that the peak height seems to increase, making the preservation of the initial amorphous state more difficult. The deformation produced by the friction and impact with the ball increases, and because of the temperature, powders may begin to show a certain tendency to crystallize.

The XRD results are similar to those reported by previous studies [24,26,36,37,39,46,53,57]. In the study reported by Bansal et al. [35], with 5:1 ball-to-ribbon ratio in a HEBM in protective atmosphere, ribbons remain amorphous after 6 h, with some traces of nanocrystals of α-Fe. When the charge ratio increases to 20:1 the milling time decreases to 1.5 h to retain the amorphous character. Likewise, Del Bianco et al. [57], with a charge ratio of 4:1 in a HEBM and a protective atmosphere, obtained, after 70 h of milling, α-Fe nanocrystals embedded in an amorphous matrix with a particle size of about 1 μm. On the other hand, Torrens-Serra et al. [31], with a charge ratio of 15:1 and a rotation speed of 200 rpm in a HEPBM, obtained α-Fe nanocrystals embedded in an amorphous matrix with a particle size larger than 45 μm after 5 h of milling. In our case, with a charge ratio of 2:1 in the VBM, and despite milling in air, a mean particle size of 47 μm is obtained after only 2.5 h of milling, and the most important, the amorphous character is mostly retained.

To corroborate these results, a TEM study was carried out. The results (Fig. 10) show the same trend as with XRD, i.e., by increasing milling time the possibility of finding particles with the presence of α-Fe

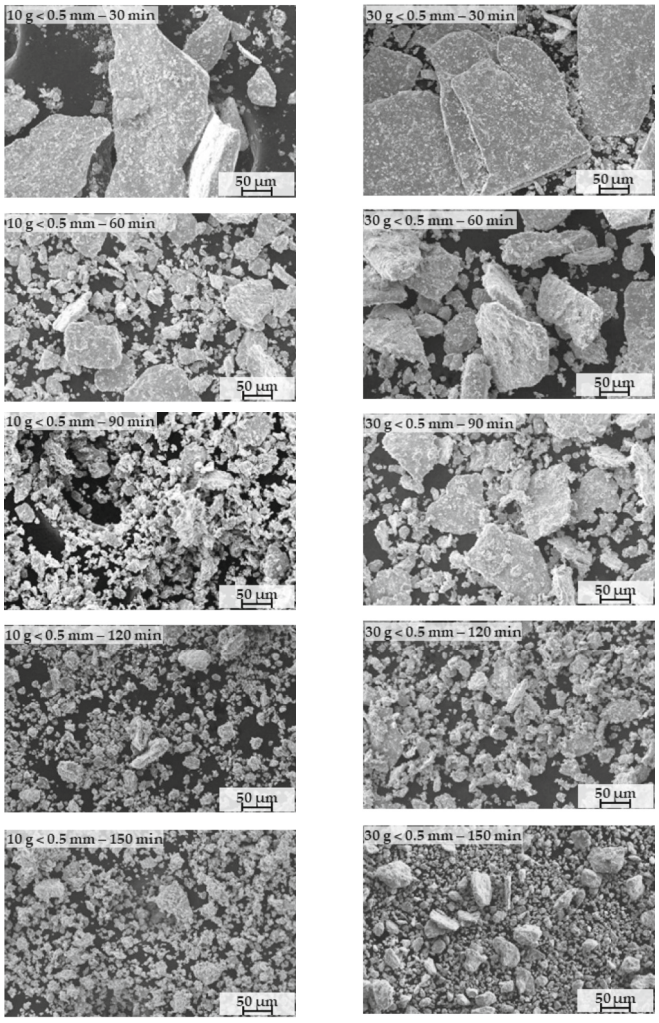

Fig. 14. SEM micrographs of powders obtained from ribbons with initial size <0.5 mm milled at 700 rpm from 30 to 150 min with vessel loads of (a) 10 g and (b) 30 g.

nanocrystals increases. It should be noted that even with prolonged milling times the existence of nanocrystalline particles is not high, especially considering that the particles characterized are the smallest, and therefore those that have received more energy during the milling process.

These TEM results agree with the results obtained by previous studies [32,53,57]. When amorphous $Fe_{78}Si_9B_{13}$ is milled under argon atmosphere, the first crystallization phase appearing is the α-Fe(Si), followed by eutectic crystallization leading to the formation of α-Fe(Si) and Fe_2B. The crystallization process and products are identical to those obtained by thermal crystallization. However, when milling is performed in air, the alloy gradually crystallizes into a single phase consisting of α-Fe(Si) nanocrystals.

In summary, XRD and TEM studies reveal that the microstructural changes after 2.5 h with the VBM are slight in terms of amorphous character, but a relatively small mean particle size, of up to 47 µm can be obtained (with 3 g of ribbons in the vessel). It should also be noted that the results obtained by TEM are relative, as only small particles, transparent to the electron beam, have been observed. These small particles could be the result of an intense deformation to reduce their size, and therefore the degree of crystallization could be higher than the milled powder as a whole.

The main drawback of the VBM is the low capacity of the equipment in terms of processed ribbons per experiment, with a maximum of 12 g. However, there are vessels on the market that can process up to 30 g per experiment.

3.2.3. *Vibratory disc mill, VDM*

The first trials on this mill were carried out loading the vessel with 10 g, at 1400 rpm (maximum of the equipment), and a milling time of 10 min (stopping 5 min after 5 min to avoid excessive heating of the vessel). The size distribution and morphology obtained for cut ribbons <0.5 mm is shown in Fig. 11.

In general, the particles lose their initial morphology and have rounded shapes. The mean particle size is d(0.5) = 54 µm, with a clear size variability. However, big particles or particles agglomerates in the order of the 1000 µm are not observed, which suggests that this could be an effect of and inefficient dispersion during the laser diffraction measurement. Thus, the actual mean size should be much smaller (based on SEM images it could be around 10 µm).

The high deformation level and small final size suggest that the amorphous character of the powder could be compromised. The analysis by XRD (Fig. 12) shows an increase in the peak intensity, corresponding to the partial crystallization of α-Fe(Si) nanocrystals. TEM shows similar

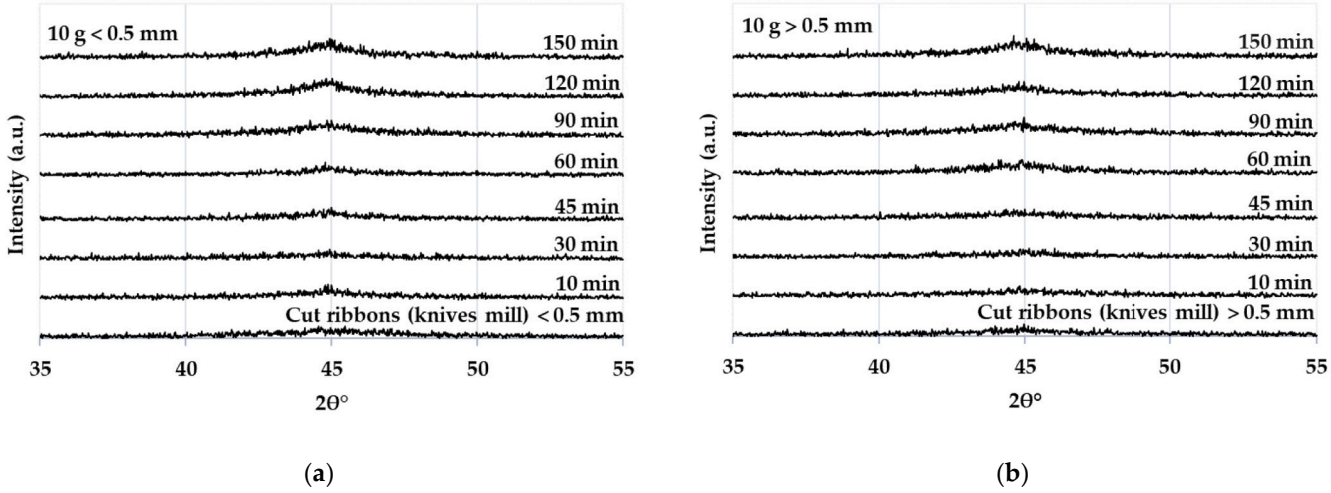

Fig. 15. XRD of $Fe_{78}Si_9B_{13}$ powder milled from the fraction (a) bigger than and (b) smaller than 0.5 mm of knife cut ribbons, with 10 g load.

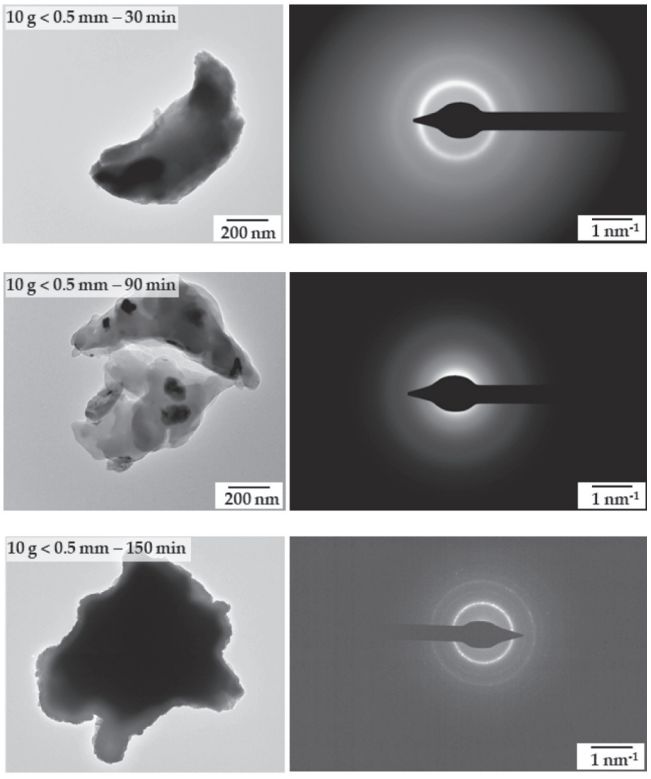

(a)

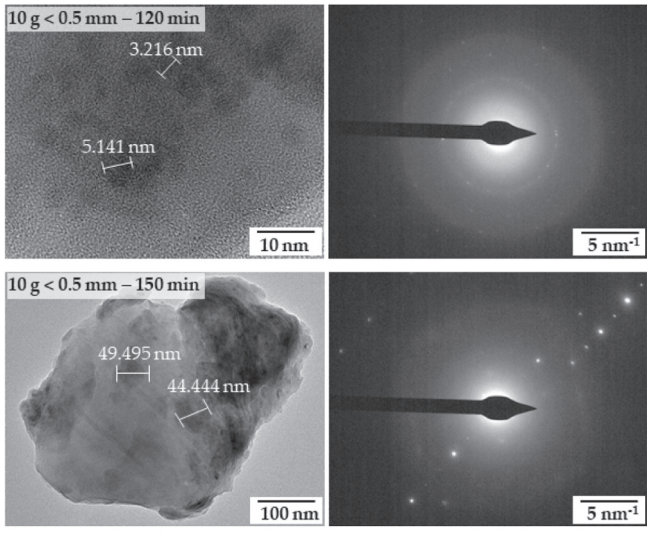

(b)

Fig. 16. **(a)** TEM image and diffraction pattern of powders obtained by milling 10 g of cut ribbons <0.5 mm from 30 to 150 min; (b) measurements of nanocrystals size.

results, even with some particles with the appearance of diffraction spots corresponding to nanocrystalline intermetallic phases, despite most of the particles remain basically amorphous.

These results show that the amorphous character is partially lost after milling, and subsequent trials were carried out with the mill at 700 rpm. To avoid excessive heating, experiments are carried out with 5-min stops every 10 min of milling.

Fig. 13 shows the granulometry of the powders obtained with vessel loads of 10 g of cut ribbons smaller and larger than 0.5 mm, for different milling times (details of the mean particle size for 10 and 30 g are also given). The combination of 30 g and cut ribbons bigger than 0.5 mm make the mill disc to slip in the vessel without milling the material correctly, and it has not been further tested.

As expected, higher milling times and lower initial particle size, make the final particle size to decrease. The minimum mean size measured is 26 μm (probably some lower in practice because double peaks can be observed due to particle agglomeration during the measuring process), and the maximum 412 μm.

SEM micrographs (Fig. 14) show that, for vessel loads of 10 and 30 g, the material conserves its flakes-shape morphology up to 60 min, starting to round off from then on. In all cases, dispersed sizes are observed, and no agglomerated particles of the size measured by laser diffraction are observed, so the agglomeration could be due to the measurement process, partially falsifying the results of average sizes.

The amorphous powders are in the form of flakes for milling times shorter than 90 min with a mill charge of 10 g, and <120 min with higher charges. For longer milling times, the particles tend to deform plastically and become rounded. The measured absolute density ranges from 6.90 g/cm^3 (mean size of 262 μm, obtained with 30 g < 0.5 mm – 30 min) to 6.74 g/cm^3 (mean size of 65 μm, obtained with 30 g < 0.5 mm – 120 min) and the tapped density from 2.58 g/cm^3 (mean size 262 μm) to 2.59 g/cm^3 (mean size 65 μm). The absolute density follows the trend observed with the VBM. The powders obtained do not flow. At a pressure of 1300 MPa the relative density varies between an 80% (mean size of 241 μm, obtained with 10 g < 0.5 mm – 10 min) and a minimum of 72% (mean size of 35 μm, obtained with 10 g < 0.5 mm – 120 min). As in the VBM, densification is higher with powders of larger mean size. It is also observed that, for the same milling time, a higher vessel charge (which makes the milling less efficient) produces a powder with higher tap density, but with almost no difference in densification, which in this case is 73% (mean size of 65 μm, obtained with 30 g < 0.5 mm – 120 min).

Regarding the microstructure, Fig. 15 shows the XRD results of some of the milled powders (results for a load of 30 g do not differ of the shown). For milling times of up to 90 min the diffractogram shows only a broad peak at $2\theta = 45^\circ$, characteristic of the amorphous state. For millings from 120 min onwards, this peak starts to appear with greater intensity, due to the presence of nanocrystals of α-Fe(Si).

The XRD agrees with studies reported by other researchers [20,24,26,36,39,50,53,54,58,59]. It has been reported that, using a HEBM with charge ratio of 20:1, rotational speed of 400 rpm and without protective atmosphere, ribbons were reduced to powder in <3 h [53]. However, by increasing the ball-to-ribbon ratio to 24:1 and the rotational speed to 750 rpm, only 45 min of milling yields to α-Fe(Si) + Fe_3B + Fe_2B + $Fe_{23}B_6$ nanocrystals embedded in an amorphous matrix with an average size of 7 μm [20,59]. A study with similar conditions reports that, to retain the amorphous character, the milling time should be <24 min in argon atmosphere [33]. At cryogenic temperatures reached with liquid N_2, amorphous powders with traces of α-Fe(Si) and Fe_2B were obtained after milling for 5 h [36]. The VDM used in this study, resembling in terms of energy provided during milling that of the HEBM or HEPBM, preserves the amorphous character in particles reaching a mean size of 35 μm after milling for 2 h with a rotational speed of 700 rpm, and without the use of protective atmospheres.

TEM shows the same result that XRD, i.e., the presence of nanocrystals increases with milling time. For milling times of 150 min, nanocrystals are larger, being more complicated to find completely amorphous zones (Fig. 16). Moreover, if the vessel load increases, the possibility of finding nanocrystalline phases decreases. In any case, the results obtained by TEM are quite relative, as only small-sized powder particles (around 500 nm), transparent to the electron beam, have been observed (while the average particle size is 50 μm, 100 times bigger). These small particles could be the result of intense milling to a smaller size, and therefore the degree of crystallization could be higher than in the whole milled powder. In the powder particles studied, the crystals

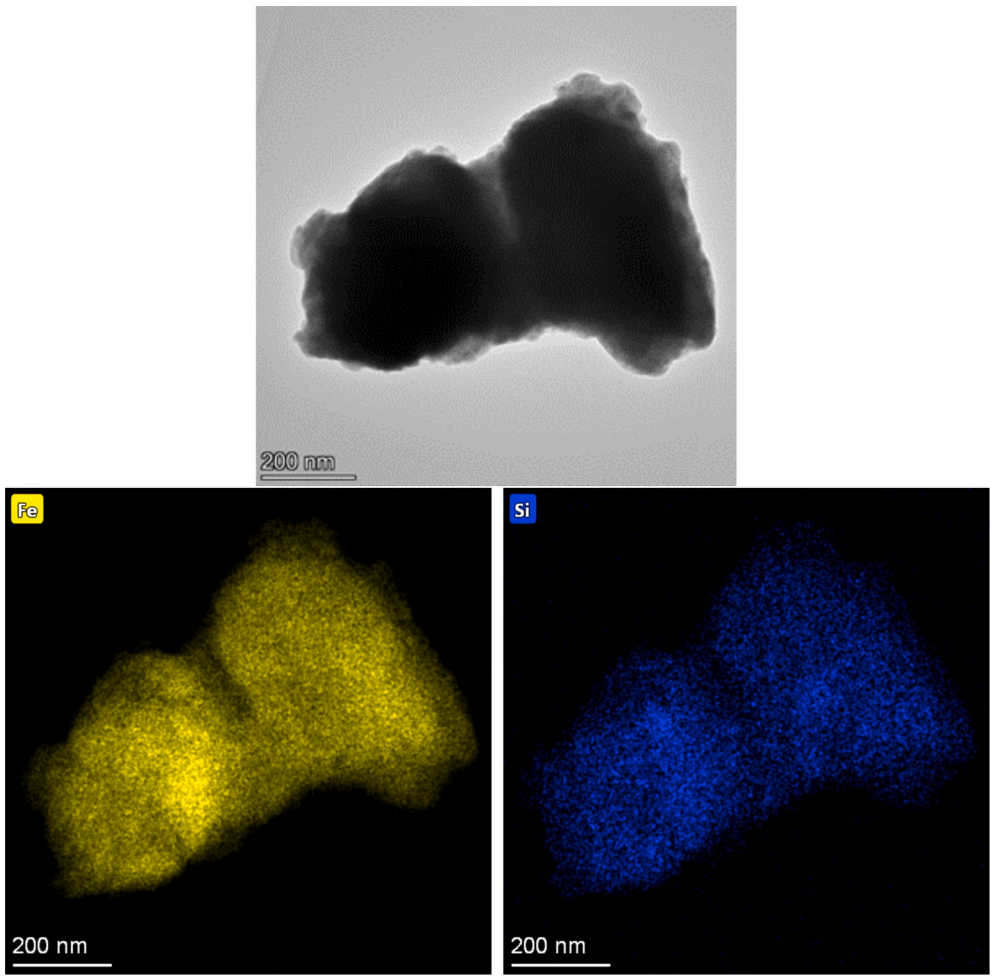

Fig. 17. EDS-STEM images of a powder particle obtained from 10 g of cut ribbon with size <0.5 mm, milled for 120 min.

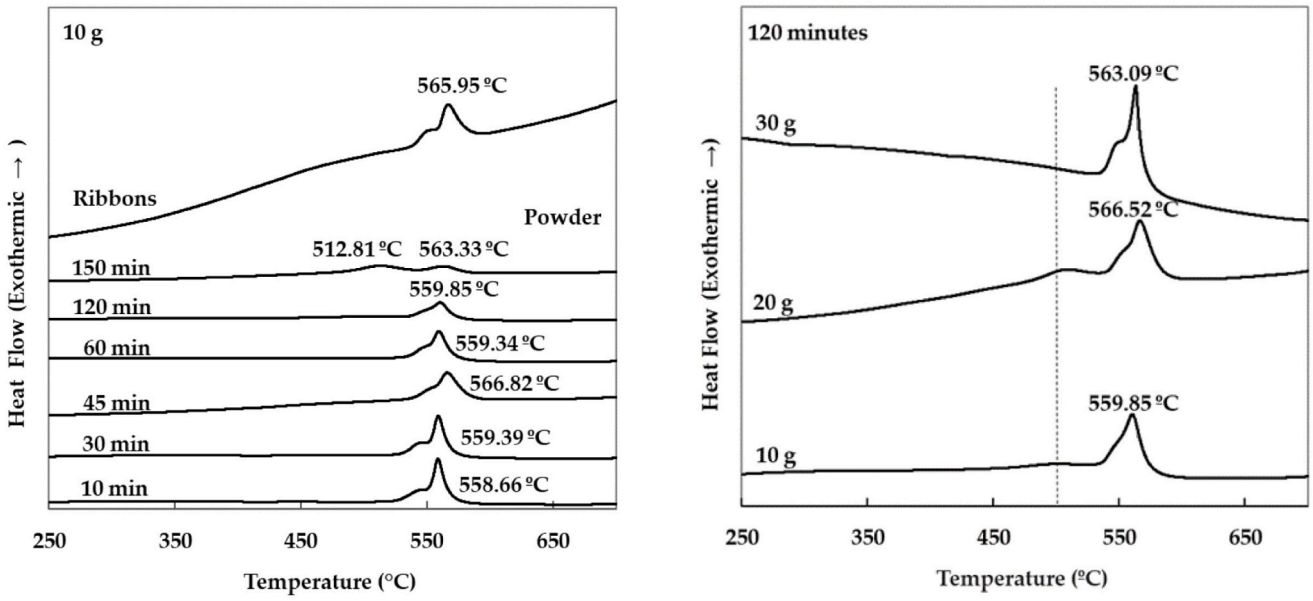

(**a**) (**b**)

Fig. 18. DSC analysis of the amorphous ribbon (0.4 mm - 28 m/s) and powders with initial size <0.5 mm milled (a) with a load of 10 g and milling times from 10 to 150 min; and (b) with a milling time of 120 min and vessel loadings of 10, 20 and 30 g.

size is in general lower than 10 nm, and only for a milling time of 150 min sizes reaching 50 nm are found.

Finally, a TEM elemental analysis is carried out to check whether or not the elements are homogeneously distributed after milling. Fig. 17 shows the distribution of Fe and Si in one of the milled particles, showing a homogeneous distribution.

The study of the crystallization process is completed with a DSC analysis (for the ribbons fraction smaller than 0.5 mm). It is found (Fig. 18) a first and very smooth (almost unappreciable) peak corresponding to the primary crystallization of α-Fe(Si), and then peaks of the secondary crystallization of Fe_2B, Fe_3B, $Fe_{23}B_6$ or Fe_2Si [32,71–80].

With a load of 10 g (Fig. 18a), for milling times up to 120 min, the two last crystallization peaks, very similar to those observed for the ribbons obtained after melt spinning, are clearly visible. The first crystallization peak occurs at temperatures around 545 °C, while the second peak is observed at temperatures between 558 and 566 °C. These results show that the powders, even with low amount of ribbons in the vessel, remain amorphous after 2 h of milling. However, a significant difference is observed in the sample milled for 150 min, probably due to the start of the crystallization during the milling process. This makes the continuation of the crystallization easier, taking place about 50 °C before (first crystallization peak at 512 °C and the second peak at 563 °C).

Analysing the influence of the vessel load for a milling time of 120 min (Fig. 18b), it is observed that for 30 g the curve is very similar to that of the original ribbons, with the primary crystallization peak at around 547 °C and the second one at around 563 °C. With 20 g, the primary crystallization of α-Fe (Si) seems to be concentrated around 500 °C, probably due to the previous onset of crystallization during milling, while the secondary crystallization peak is at a similar temperature to that of the original ribbons, namely at 566 °C. Finally, at 10 g load, the primary crystallization is less evident, which would indicate that more primary crystallization has occurred previously, and the secondary crystallization peak is at 559 °C. These results corroborate the conclusions drawn from the XRD and TEM studies discussed previously.

Therefore, to preserve the amorphous character in the powders with the VDM at 700 rpm, and with vessel loads of up to 10 g, the milling time should not exceed 120 min, always with stops of 5 min every 10 min of milling. By increasing the load, the amorphous state is more easily preserved.

4. Conclusions

The melt spinning process has been used to produce amorphous $Fe_{78}Si_9B_{13}$ ribbons in discontinuous lab scale experiments, with a process efficiency around 90%. The ribbons are milled to powder in two types of vibratory mills that normally are not used for this purpose (VBM and VDM). Both mills allow reaching a powder particle size adequate for PM processing, at the time that maintaining the amorphous microstructure necessary for magnetic applications. The milling processes can be carried out in air, without the need of using protective atmospheres.

As compared to the most extended types of mills used (high energy ball mills and planetary ball mills) the necessary time to reach a proper powder particle size for PM has been relatively short: 90 min in the VBM with a vessel load of 3 g, and 40 min in the VDM with a charge of 10 g, to reach a mean size of 90 μm. Smaller particle sizes can be reached by milling for longer times: 47 and 26 μm after 150 min in the VBM and VDM, respectively.

The efficiency of these milling processes is around 99% and being unnecessary the use of milling process control agents, the obtained powder is free of contamination.

No crystallization occurred in the powders with sizes of up to 48 μm, showing two exothermic reactions during DSC heating, due to the crystallization of α-Fe(Si) and intermetallics formation. Highly-deformed finer powders show, after milling, traces of nanocrystals of the α-Fe(Si) phase, being however the amorphous structure clearly predominant after milling for 120 min.

According to this, the VDM can produce amorphous $Fe_{78}Si_9B_{13}$ powders from amorphous ribbons in a shorter time and with higher vessel loads.

It is concluded that the studied VBM and VDM, and the associated milling processes, are appropriate to obtain amorphous powder from melt spinning ribbons, ready for use by PM methods. The sizes of the obtained powders are in the same order of those obtained with the extensively used HEBM and HEPBM, being necessary even shorter times.

Funding

This research was funded by Ministerio de Economía y Competitividad (Spain) and Feder (EU) through the research project PID2021-123750-OB-I00, and research support conceded by the University of Huelva.

Funding for open access charge: Universidad de Huelva / CBUA

CRediT authorship contribution statement

Rosa María Aranda: Writing – review & editing, Writing – original draft, Visualization, Validation, Supervision, Resources, Methodology, Investigation, Conceptualization. **Raquel Astacio:** Writing – review & editing, Validation. **Petr Urban:** Writing – review & editing, Validation. **Beatriz Aranda:** Writing – review & editing, Validation. **Francisco G. Cuevas:** Writing – review & editing, Writing – original draft, Methodology, Conceptualization.

Declaration of competing interest

The authors declare no conflict of interest. The funders had no role in the design of the study; in the collection, analyses, or interpretation of data; in the writing of the manuscript, or in the decision to publish the results.

Data availability

No data was used for the research described in the article.

Acknowledgments

The authors also wish to thank the technicians M. Sánchez, J. Pinto, C. Cerrillo and F. Varela (University of Seville, Spain), C. Cantero and C. Lara (University of Huelva, Spain) for experimental assistance.

References

[1] J.C. Qiao, Q. Wang, J.M. Pelletier, H. Kato, R. Casalini, D. Crespo, E. Pineda, Y. Yao, Y. Yang, Structural heterogeneities and mechanical behavior of amorphous alloys, Intermetallics 94 (2018) 65–72, https://doi.org/10.1016/j.pmatsci.2019.04.005.

[2] H.R. Lashgari, D. Chu, S. Xie, H. Sun, M. Ferry, S. Li, Composition dependence of the microstructure and soft magnetic properties of Fe-based amorphous/nanocrystalline alloys: a review study, J. Non-Cryst. Solids 391 (2014) 61–82, https://doi.org/10.1016/j.jnoncrysol.2014.03.010.

[3] D.D. Coimbrão, G. Zepon, G.Y. Koga, D.A. Godoy Pérez, F.H. Paes de Almeida, V. Roche, J.-C. Lepretre, A.M. Jorge, C.S. Kiminami, C. Bolfarini, A. Inoue, W. J. Botta, Corrosion properties of amorphous, partially, and fully crystallized $Fe_{68}Cr_8Mo_4Nb_4B_{16}$ alloy, J. Alloys Compd. 826 (2020) 154123, https://doi.org/10.1016/j.jallcom.2020.154123.

[4] F.G. Cuevas, S. Lozano-Perez, R.M. Aranda, R. Astacio, Crystallization process and microstructural evolution of melt spun Al-RE-Ni-(Cu) ribbons, Metals 10 (4) (2020) 443, https://doi.org/10.3390/met10040443].

[5] K.L. Alvarez, J.M. Martín, N. Burgos, M. Ipatov, L. Domínguez, J. González, Structural and magnetic properties of amorphous and nanocrystalline Fe–Si–B–P–Nb–Cu alloys produced by gas atomization, J. Alloys Compd. 810 (2019) 151754, https://doi.org/10.1016/j.jallcom.2019.151754.

[6] B. Huang, C. Zhang, G. Zhang, H. Liao, Wear and corrosion resistant performance of thermal-sprayed Fe-based amorphous coatings: a review, Surf. Coat. Technol. 377 (2019) 124896, https://doi.org/10.1016/j.surfcoat.2019.124896.

[7] O. Camara, M.A. Tunes, G. Greaves, A.H. Mir, S. Donnelly, J.A. Hinks, Understanding amorphization mechanisms using ion irradiation in situ a TEM and

3D damage reconstruction, Ultramicroscopy 207 (2019) 112838, https://doi.org/10.1016/j.ultramic.2019.112838.
[8] K. Van Stiphout, F.A. Geenen, N.M. Santos, S.M.C. Miranda, V. Joly, J. Demeulemeester, C. Detavernier, F. Kremer, L.M.C. Pereira, K. Temst, A. Vantomme, Impurity-enhanced solid-state amorphization: the Ni-Si thin film reaction altered by nitrogen, J. Phys. D: Appl. Phys. 52 (14) (2019) 145301, https://doi.org/10.1088/1361-6463/ab00d2.
[9] P. Urban, F. Ternero, E.S. Caballero, S. Nandyala, J.M. Montes, F.G. Cuevas, Amorphous Al-Ti powders prepared by mechanical alloying and consolidated by electrical resistance sintering, Metals 9 (2019) 1140, https://doi.org/10.3390/met9111140.
[10] W. Lu, B. Yan, R. Tang, Bulk metglas, finemet and nanoperm soft magnetic alloys prepared by ultra-high-pressure consolidation, J. Alloys Compd. 425 (2006) 406–410, https://doi.org/10.1016/j.jallcom.2006.01.063.
[11] A. Inoue, F.L. Kong, Q.K. Man, B.L. Shen, R.W. Li, F. Al-Marzouki, Development and applications of Fe- and co-based bulk glassy alloys and their prospects, J. Alloys Compd. 615 (2014) S2–S8, https://doi.org/10.1016/j.jallcom.2013.11.122.
[12] Z. Mahbooba, L. Thorsson, M. Unosson, P. Skoglund, H. West, T. Horn, C. Rock, E. Vogli, O. Harrysson, Additive manufacturing of an iron-based bulk metallic glass larger than the critical casting thickness, Appl. Mater. Today 11 (2018) 264–269, https://doi.org/10.1016/j.apmt.2018.02.011.
[13] F. Ren, L. Ward, T. Williams, K.J. Laws, C. Wolverton, J. Hattrick-Simpers, A. Mehta, Accelerated discovery of metallic glasses through iteration of machine learning and high-throughput experiments, Sci. Adv. 4 (4) (2018) 1566, https://doi.org/10.1126/sciadv.aaq1566.
[14] R. Ma, P. Yu, The influences of matrix materials on the magnetic and mechanical properties of $Fe_{78}Si_9B_{13}$ soft magnetic composites fabricated by injection molding, Mater. Res. Bull. 139 (2021) 111256, https://doi.org/10.1016/j.materresbull.2021.111256.
[15] E.A. Olevsky, D.V. Dudina, Field-assisted sintering, in: Sci. Appl, Springer, Switzerland, 2018, https://doi.org/10.1007/978-3-319-76032-2.
[16] R.S. Maurya, A. Sahu, T. Laha, Effect of consolidation pressure on phase evolution during sintering of mechanically alloyed $Al_{86}Ni_8Y_6$ amorphous powders via spark plasma sintering, Mater. Sci. Eng. A 649 (2016) 48–56, https://doi.org/10.1016/j.msea.2015.09.109.
[17] A. Sahu, R.S. Maurya, T. Laha, Comparative study on sintering behavior of $Al_{86}Ni_6Y_{4.5}Co_2La_{1.5}$ mechanically alloyed amorphous powder and melt-spun ribbon, Adv. Powder Technol. 30 (4) (2019) 691–699, https://doi.org/10.1016/j.apt.2018.12.019.
[18] A. Michalcová, T. Bastl, A. Knaislová, I. Marek, The influence of rapidly solidified ribbons pre-treatment on structure of bulk AlFeMm alloys prepared by Powder Metallurgy, Manuf. Technol. 18 (4) (2018) 621–624, https://doi.org/10.21062/ujep/149.2018/a/1213-2489/MT/18/4/621.
[19] M. Srinivas, A. Paradkar, B.S. Murty, B. Majumdar, Processing of $[(Fe_{0.5}Co_{0.5})_{0.75}B_{0.2}Si_{0.05}]_{96}Nb_4$ bulk metallic glass alloy by Cu mould casting and spark plasma sintering, Trans. Indian Inst. Metals 71 (2) (2018) 309–317, https://doi.org/10.1007/s12666-017-1183-x.
[20] T. Gheiratmand, H.R. Madaah Hosseini, P. Davami, C. Sarafidis, Fabrication of FINEMET bulk alloy from amorphous powders by spark plasma sintering, Powder Technol. 289 (2016) 163–168, https://doi.org/10.1016/j.powtec.2015.11.060.
[21] P. Urban, F. Ternero, E.S. Caballero, S. Nandyala, J.M. Montes, F.G. Cuevas, Amorphous Al-Ti powders prepared by mechanical alloying and consolidated by electrical resistance sintering, Metals 9 (2019) 1140, https://doi.org/10.3390/met9111140.
[22] R.M. Aranda, F. Ternero, S. Lozano-Pérez, J.M. Montes, F.G. Cuevas, Capacitor electrical discharge consolidation of metallic powders—a review, Metals 11 (2021) 616, https://doi.org/10.3390/met11040616.
[23] C. Suryanarayana, In situ mechanical crystallization of amorphous alloys, J. Alloys Compd. 961 (2023) 171032, https://doi.org/10.1016/j.jallcom.2023.171032.
[24] M.L. Trudeau, R. Schulz, D. Dussault, A. Van Neste, Structural changes during high-energy ball milling of iron-based amorphous alloys: is high-energy ball milling equivalent to a thermal process? Phys. Rev. Lett. 64 (1) (1990) 99–102, https://doi.org/10.1103/PhysRevLett.64.99.
[25] M.L. Trudeau, J.Y. Huot, R. Schulz, D. Dussault, A. Van Neste, G. L'Espérance, Nanocrystalline Fe-(Co,Ni)-Si-B: The mechanical crystallization of amorphous alloys and the effects on electrocatalytic reactions, Phys. Rev. B 45 (9) (1992) 4626–4636, https://doi.org/10.1103/PhysRevB.45.4626.
[26] M.L. Trudeau, L. Dignard-Bailey, R. Schulz, D.A. Van Dussault, Neste, Fabrication of nanocrystalline iron-based alloys by the mechanical crystallization of amorphous materials, Nanostruct. Mater. 2 (1993) 361–368, https://doi.org/10.1016/0965-9773(93)90177-D.
[27] Z. Yan, Y. Liu, S. Pan, Y. Hu, J. Pang, W. Wang, The structural evolution of $Al_{86}Ni_9La_5$ glassy ribbons during milling at room and cryogenic temperatures, Materials 11 (10) (2018) 1956, https://doi.org/10.3390/ma11101956.
[28] H. Ghayour, M. Abdellahi, M. Bahmanpour, Optimization of the high energy ball-milling: modeling and parametric study, Powder Technol. 291 (2016) 7–13, https://doi.org/10.1016/j.powtec.2015.12.004.
[29] D.V. Dudina, B.B. Bokhonov, Materials development using high-energy ball milling: a review dedicated to the memory of M.A. Korchagin, J. Compos. Sci. 6 (2022) 188, https://doi.org/10.3390/jcs6070188.
[30] K.V. Nagesha, D. Arunkumar, G.M. Kumar, R. Yadav, U. Khakha, B. Vishwakarma, Renu., Parametric study on four station ball mill for synthesis of ultrafine powders, Mater. Today Proc. (2023), https://doi.org/10.1016/j.matpr.2023.04.360.
[31] J. Torrens-Serra, P. Bruna, S. Roth, J. Rodriguez-Viejo, M.T. Clavaguera-Mora, Bulk soft magnetic materials from ball-milled $Fe_{77}Nb_7B_{15}Cu_1$ amorphous ribbons, Intermetallics 17 (2009) 79–85, https://doi.org/10.1016/j.intermet.2008.10.002.
[32] J. Torrens-Serra, S. Roth, J. Rodriguez-Viejo, M.T. Clavaguera-Mora, Structure and thermomagnetic properties of powders produced from melt spun FeNbBCu ribbons, J. Non-Cryst. Solids 354 (2008) 3858–3863, https://doi.org/10.1016/j.jnoncrysol.2008.05.007.
[33] T. Gheiratmand, H.R. Madaah Hosseini, P. Davami, G. Ababei, M. Song, Mechanism of mechanically induced nanocrystallization of amorphous FINEMET ribbons during milling, Metall. Mater. Trans. A 46 (2015) 2718–2725, https://doi.org/10.1007/s11661-015-2848-x.
[34] D. Oleszak, D. Kolesnikov, T. Kulik, $Ni_{59}Zr_{20}Ti_{16}Si_5$ bulk amorphous alloy obtained by mechanical alloying and powder consolidation, Mat. Sci. Eng.: A 449–451 (2007) 1127–1130, https://doi.org/10.1016/j.msea.2006.02.270.
[35] C. Bansal, B. Fultz, W.L. Johnson, Crystallization of $Fe_{78}B_9Si_{13}$ metallic glass during ball milling, Nanostruct. Mater. 4 (8) (1994) 919–925, https://doi.org/10.1016/0965-9773(94)90098-1.
[36] B.L. Huang, R.J. Perez, P.J. Crawford, S.R. Nutt, E.J. Lavernia, Mechanical crystallization of Metglas $Fe_{78}B_{13}Si_9$ by cryogenic high energy ball milling, MRS Symp. Proc. 400 (1995) 227–232, https://doi.org/10.1557/PROC-400-227.
[37] S. Flohrer, R. Schäfer, C. Polak, G. Herzer, Interplay of uniform and random anisotropy in nanocrystalline soft magnetic alloys, *Acta Mater.* 53 (10) (2005) 2937–2942, https://doi.org/10.1016/j.actamat.2005.03.008.
[38] T. Kulik, G. Vlasák, R. Żuberek, Correlation between microstructure and magnetic properties of amorphous and nanocrystalline $Fe_{73.5}Cu_1Nb_3Si_{16.5}B_6$, Mater. Sci. Eng. A 226–228 (1997) 701–705, https://doi.org/10.1016/S0921-5093(97)80074-3.
[39] H. Pak, J. Chu, R.J. Deangelis, K. Okazaki, Phase transitions in mechanically comminuted $Fe_{78}B_{13}Si_9$ amorphous ribbon, Mater. Sci. Eng. A 118 (1989) 147–153, https://doi.org/10.1016/0921-5093(89)90067-1.
[40] F.Q. Guo, K. Lu, Ball-milling-induced crystallization and ball-milling effect on thermal crystallization kinetics in an amorphous FeMoSiB alloy, Metall. Mater. Trans. A 28 (1997) 1123–1131, https://doi.org/10.1007/s11661-997-0278-0.
[41] G.J. Fan, M.X. Quan, Z.Q. Hu, W. Loser, J. Eckert, Deformation-induced microstructural changes in $Fe_{40}Ni_{40}P_{14}B_6$ metallic glass, J. Mater. Res. 149 (1999) 3765–3774, https://doi.org/10.1557/JMR.1999.0510.
[42] H. Xu, K.Y. He, Y.Q. Qiu, Z.J. Wang, W. Feng, Y.D. Dong, X.S. Xiao, Q. Wang, Intense milling nanocrystalline $Fe_{73.5}Cu_1Nb_3Si_{13.5}B_9$: a soft magnetic material in powdered form, Mater. Sci. Eng. A 286 (1) (2000) 197–200, https://doi.org/10.1016/S0921-5093(00)00713-9.
[43] J. Degmova, S. Roth, J. Eckert, H. Grahl, L. Schultz, Magnetic properties of bulk amorphous FeAlGaPCBSi samples prepared by ball-milling and subsequent hot pressing, Mater. Sci. Eng. A 375–377 (2004) 265–269, https://doi.org/10.1016/j.msea.2003.10.023.
[44] J. Sort, D.C. Ile, A.P. Zhilyaev, A. Concustell, T. Czeppe, M. Stoica, S. Suriñach, J. Eckert, M.D. Baró, Cold-consolidation of ball-milled Fe-based amorphous ribbons by high pressure torsion, Scr. Mater. 50 (9) (2004) 1221–1225, https://doi.org/10.1016/j.scriptamat.2004.02.004.
[45] J.J. Suñol, A. González, T. Pradell, P. Bruna, M.T. Clavaguera-Mora, N. Clavaguera, Thermal and structural changes induced by mechanical alloying in melt-spun Fe–Ni based amorphous alloys, Mater. Sci. Eng. A 375–377 (2004) 881–887, https://doi.org/10.1016/j.msea.2003.10.195.
[46] R. Nowosielski, J.J. Wysłocki, I. Wnuk, P. Sakiewicz, P. Gramatyka, Ferromagnetic properties of polymer nanocomposites containing $Fe_{78}Si_9B_{13}$ powder particles, J. Mater. Process. Technol. 162–163 (2005) 242–247, https://doi.org/10.1016/j.jmatprotec.2005.02.010.
[47] W. Lu, L. Yang, B. Yan, W. Huang, Mechanically driven nanocrystallization of amorphous $Fe_{73.5}Cu_1Nb_3Si_{13.5}B_9$ alloy induced by high-energy ball milling, Phys. Status Solidi 202 (2005) 1733–1739, https://doi.org/10.1002/pssa.200420038.
[48] A. Grabias, D. Oleszak, J. Kalinowska, M. Kopcewicz, J. Latuch, M. Pękała, Structure of the nanocrystalline $Fe_{41}Ni_{20}Co_{20}Zr_7B_{12}$ alloy formed by ball milling, J. Alloys Compd. 434–435 (2007) 493–496, https://doi.org/10.1016/j.jallcom.2006.08.122.
[49] B.G. Moon, K.Y. Sohn, W.W. Park, T.D. Lee, Effect of milling on the soft magnetic behavior of nanocrystalline alloy cores, Mater. Sci. Eng. A 448–451 (2007) 426–429, https://doi.org/10.1016/j.msea.2005.12.103.
[50] J. Ipus, J.S. Blázquez, V. Franco, A. Conde, Ball milling of $Fe_{83}Zr_6B_{10}Cu_1$ amorphous alloy containing quenched in crystals, Intermetallics 15 (8) (2007) 1132–1138, https://doi.org/10.1016/j.intermet.2007.02.003.
[51] M. López, P. Marín, P. Agudo, I. Carabias, J. de la Venta, A. Hernando, Nanocrystalline FeSiBNbCu alloys: differences between mechanical and thermal crystallization process in amorphous precursors, J. Alloys Compd. 434–435 (2007) 199–202, https://doi.org/10.1016/j.jallcom.2006.08.127.
[52] P.P. Choi, I.V. Povstugar, Y.S. Kwon, E.P. Yelsukov, J.S. Kim, Ball milling induced crystallization of amorphous $Fe_{90}Zr_{10}$, Mater. Sci. Eng. A 449–451 (2007) 1079–1082, https://doi.org/10.1016/j.msea.2006.02.266.
[53] Z. Changqin, Z. Zhonghua, Q. Zhen, Q. Yongxin, Z. Junyan, B. Xiufang, Ball milling induced abnormal crystallization behavior of an amorphous $Fe_{78}Si_9B_{13}$ alloy, J. Non-Cryst. Solids 354 (32) (2008) 3812–3816, https://doi.org/10.1016/j.jnoncrysol.2008.05.003.
[54] Z. Xiao, C. Tang, H. Zhao, D. Zhang, Y. Li, Effects of sintering temperature on microstructure and property evolution of $Fe_{81}Cu_2Nb_3Si_{14}$ soft magnetic materials fabricated from amorphous melt-spun ribbons by spark plasma sintering technique, J. Non-Cryst. Solids 358 (1) (2012) 114–118, https://doi.org/10.1016/j.jnoncrysol.2011.09.001.

[55] Y. Geng, T. Ablekim, P. Mukherjee, M. Weber, K. Lynn, J.E. Shield, High-energy mechanical milling-induced crystallization in $Fe_{32}Ni_{52}Zr_3B_{13}$, J. Non-Cryst. Solids 404 (2014) 140–144, https://doi.org/10.1016/j.jnoncrysol.2014.08.015.
[56] H. Chiriac, N. Lupu, M. Lostun, G. Ababei, M. Grigoraş, C. Danceanu, Low TC Fe-Cr-Nb-B glassy submicron powders for hyperthermia applications, J. Appl. Phys. 115 (2014) 2014–2017.
[57] L. Del Bianco, F. Spizzo, A. Deriu, A. Orecchini, Inelastic neutron scattering investigation of ball-milled FeSiB described as a magnetic nanoglass-like structure, J. Alloys Compd. 615 (1) (2014) S224–S227, https://doi.org/10.1016/j.jallcom.2013.10.125.
[58] M.L. Prasanna, B. Majumdar, V.L. Niranjani, S.V. Kamat, Microstructure and mechanical properties of $[(Fe_{0.5}Co_{0.5})_{0.75}B_{0.2}Si_{0.05}]_{96}Nb_4$ bulk metallic glass compacts, Trans. Indian Inst. Metals 68 (2015) 1033–1037, https://doi.org/10.1007/s12666-015-0642-5.
[59] T. Gheiratmand, H.R. Madaah Hosseini, P. Davami, M. Gjoka, M. Song, The effect of mechanical milling on the soft magnetic properties of amorphous FINEMET alloy, J. Magn. Magn. Mater. 381 (2015) 322–327, https://doi.org/10.1016/j.jmmm.2015.01.016.
[60] P. Ramasamy, R.N. Shahid, S. Scudino, J. Eckert, M. Stoica, Influencing the crystallization of $Fe_{80}Nb_{10}B_{10}$ metallic glass by ball milling, J. Alloys Compd. 725 (2017) 227–236, https://doi.org/10.1016/j.jallcom.2017.07.160.
[61] B. Zhang, Y. Duan, X. Yang, G. Ma, T. Wang, X. Dong, Y. Zeng, Tuning magnetic properties based on $FeCoNiSi_{0.4}Al_{0.4}$ with dual-phase nano-crystal and nano-amorphous microstructure, Intermetallics 117 (2020) 106678, https://doi.org/10.1016/j.intermet.2019.106678.
[62] K. Liu, S. Wang, Y. Feng, K. Zhang, Y. Zhang, Phase transformation mechanism and magnetic properties of Sm-Fe alloys produced by melt-spinning and high-energy ball milling, J. Magn. Magn. Mater. 513 (2020) 167229, https://doi.org/10.1016/j.jmmm.2020.167229.
[63] Y. Ma, L. Xie, Q. Li, C. Chang, H. Li, B. Mu, X. Ma, Influence of surface morphology of Fe-based amorphous alloys on degradation of azo dye, J. Phys. Chem. Solids 163 (2022) 110596, https://doi.org/10.1016/j.jpcs.2022.110596.
[64] A. Inoue, F. Kong, *Soft* Magn. Mater., Encyclopedia of Smart Materials; Abdul-Ghani Olabi, Elsevier, 2022, pp. 10–23, https://doi.org/10.1016/B978-0-12-803581-8.11725-4.
[65] ISO 3953:2011, Metallic powders. Determination of tap density, International Organization for Standardization [ISO], 2011.
[66] ISO 4490:2018, Metallic powders. Determination of flow rate by means of a calibrated funnel (Hall flowmeter), International Organization for Standardization [ISO], 2018.
[67] ISO 3927:2017, Metallic powders. excluding powders for hard metal. Determination of compressibility in uniaxial compression, International Organization for Standardization [ISO], 2017.
[68] X.Y. Cui, S.P. Ringer, G. Wang, Z.H. Stachurski, What should the density of amorphous solids be? J. Chem. Phys. 151 (2019) 194506 https://doi.org/10.1063/1.5113733.
[69] Metglas®, Inc., in https://metglas.com/, date of access 7 april 2024.
[70] S. Scudino, S. Venkataraman, M. Stoica, K.B. Surreddi, S. Pauly, J. Das, J. Eckert, Consolidation and mechanical properties of ball milled $Zr_{50}Cu_{50}$ glassy ribbons, J. Alloys Compd. 483 (1–2) (2009) 227–230, https://doi.org/10.1016/j.jallcom.2008.07.149.
[71] Z.H. Sheng, J. Pang, X. Wang, K. Wen, L.Y. Guo, K.B. Kim, W.M. Wang, Anisotropic magnetization improvement in $Fe_{78}Si_9B_{13}$ glass with direct current heating, J. Non-Cryst. Solids 448 (2016) 83–88, https://doi.org/10.1016/j.jnoncrysol.2016.07.006.
[72] N. Eliaz, D. Eliezer, Hydrogen effects on an amorphous Fe-Si-B alloy, Metall. Mater. Trans. A 31 (10) (2000) 2517–2526, https://doi.org/10.1007/s11661-000-0196-x.
[73] T. Naohara, Aging behavior of the microstructure and soft magnetic properties in amorphous Fe-Si-B-Nb alloys, J. Appl. Phys. 79 (10) (1996) 7926–7930, https://doi.org/10.1063/1.362406.
[74] W.M. Wang, S.F. Jin, J.T. Zhang, T. Huang, L. Wang, X.F. Bian, Microstructure evolution in the rapidly quenched $Fe_{78}Si_9B_{13}$ ribbons, Phys. B Condens. Matter 404 (20) (2009) 3413–3416, https://doi.org/10.1016/j.physb.2009.05.024.
[75] H.Y. Tong, J.T. Wang, B.Z. Ding, H.G. Jiang, K. Lu, The structure and properties of nanocrystalline $Fe_{78}B_{13}Si_9$ alloy, J. Non-Cryst. Solids 150 (1) (1992) 444–447, https://doi.org/10.1016/0022-3093(92)90169-K.
[76] C.F. Chang, J. Marti, Crystallization of the metallic glass $Fe_{80}B_{12}Si_8$, J. Mater. Sci. 18 (8) (1983) 2297–2304, https://doi.org/10.1007/BF00541833.
[77] J.C. Rawers, R.A. McCune, A. Adams, Crystallization of amorphous $Fe_{78}B_{13}Si_9$, J. Mater. Sci. Lett. 7 (9) (1988) 958–960. https://api.semanticscholar.org/CorpusID:138378205.
[78] S.U. Jen, C.Y. Lee, Crystallization in amorphous $Fe_{78}B_{13}Si_9$, J. Magn. Magn. Mater. 89 (1) (1990) 214–220, https://doi.org/10.1016/0304-8853(90)90729-A.
[79] S.U. Jen, Isothermal crystallization of amorphous $Fe_{78}B_{13}Si_9$, Mater. Sci. Eng. A 133 (1991) 479–481, https://doi.org/10.1016/0921-5093(91)90114-3.
[80] J.Y. Bang, R.Y. Lee, Crystallization of the metallic glass $Fe_{78}B_{13}Si_9$, J. Mater. Sci. 26 (18) (1991) 4961–4965, https://doi.org/10.1007/BF00549877.